

Imaging the lithosphere–asthenosphere boundary beneath the Pacific using SS waveform modeling

Catherine A. Rychert¹ and Peter M. Shearer²

Received 27 October 2010; revised 13 April 2011; accepted 19 April 2011; published 28 July 2011.

[1] Oceanic lithosphere constitutes the bulk of Earth's tectonic plates and also likely represents the building blocks of the continental lithosphere. The depth and nature of the oceanic lithosphere–asthenosphere boundary are central to our understanding of the definition of the tectonic plates and lithospheric evolution. Although it is well established that oceanic lithosphere cools, thickens, and subsides as it ages according to conductive cooling models, this relatively simple realization of the tectonic plates is not completely understood. Old (>70 Ma) ocean depths are shallower than predicted. Furthermore, precise imaging of the lower boundary of the oceanic lithosphere has proven challenging. Here we directly map the depth and nature of a seismic discontinuity that is likely the lithosphere–asthenosphere boundary across the Pacific plate using a new method that models variations in the shapes of stacked SS waveforms from 17 years of seismic data. The depth to the discontinuity varies from 25 to 130 km and correlates with distance from the ridge along mantle flow lines. This implies that the depth of the oceanic lithosphere–asthenosphere boundary depends on the temperature of the underlying asthenosphere, defined by a best fitting isotherm at 930°C with a 95% confidence region of 820–1020°C, although the sharpness of the observations in some locations implies a mechanism besides temperature may also be required.

Citation: Rychert, C. A., and P. M. Shearer (2011), Imaging the lithosphere–asthenosphere boundary beneath the Pacific using SS waveform modeling, *J. Geophys. Res.*, 116, B07307, doi:10.1029/2010JB008070.

1. Introduction

[2] Seafloor subsides according to conductive cooling models up until ~70 MA as indicated by gravity, heat flow, depth of seismicity, and seismic imaging [Parsons and Sclater, 1977; Watts, 1978; Nishimura and Forsyth, 1989; Stein and Stein, 1992], but older lithosphere is generally shallower than predicted by these models. The reason for the deviation is hypothesized to be an additional heat source, possibly caused by small-scale instabilities or hot spot alteration [Parsons and Sclater, 1977; Stein and Stein, 1992; Smith and Sandwell, 1997; Korenaga and Korenaga, 2008]. However, the behavior of old oceanic lithosphere has remained an outstanding topic of debate, and it has recently been proposed that seafloor subsidence is more closely related to the distance from the ridge along current mantle flow lines; that is, the lithosphere readjusts to the state of the underlying asthenosphere [Adam and Vidal, 2010].

[3] The thickness of the lithosphere likely follows the observed pattern of subsidence. However, direct measurements of the thickness and defining mechanism of this system have proven difficult. Surface waves resolve thickening

of the seismically fast lid with seafloor age over the entire Pacific plate [Nishimura and Forsyth, 1989; Ritzwoller et al., 2004; Maggi et al., 2006; Nettles and Dziewoński, 2008] and on a regional scale from the East Pacific Rise to a distance ~700 km to the west [Harmon et al., 2009] and in combination with body waves beneath the eastern Pacific Ocean Ridges [Gu et al., 2005], although not with enough depth resolution to test hypotheses regarding the nature of the transition from the lithosphere to the underlying asthenosphere. A receiver function study of oceanic lithosphere found a sharp seismic discontinuity (7–8% over 10–15 km) with a positive age–depth trend that was interpreted as partial melting of the asthenosphere, though on a local scale, with two observation points on the Philippine plate and one on the Pacific plate [Kawakatsu et al., 2009]. The trend was recently confirmed by receiver function constraints on the thickness of subducting lithosphere from land stations at the Japan, Aleutian, and North American ocean–continent plate boundaries [Kumar and Kawakatsu, 2011]. Finally, a significant (4.7–14.3%) seismic discontinuity at constant depth beneath the seafloor (63–80 km depending on the study) has also been reported for large swaths of the Pacific from studies using combinations of ScS reflectivity profiles, multiple S bounces, and surface waves [Gaherty et al., 1999; Tan and Helmberger, 2007; Bagley and Revenaugh, 2008], and interpreted as frozen-in structure related to lithospheric formation at the ridge or partial melting of the deeper layer. Overall, a seismic discontinuity associated with the lithosphere–asthenosphere boundary (LAB) has yet to be mapped

¹Department of Earth Science, University of Bristol, Bristol, UK.

²Institute of Geophysics and Planetary Physics, Scripps Institution of Oceanography, University of California, San Diego, La Jolla, California, USA.

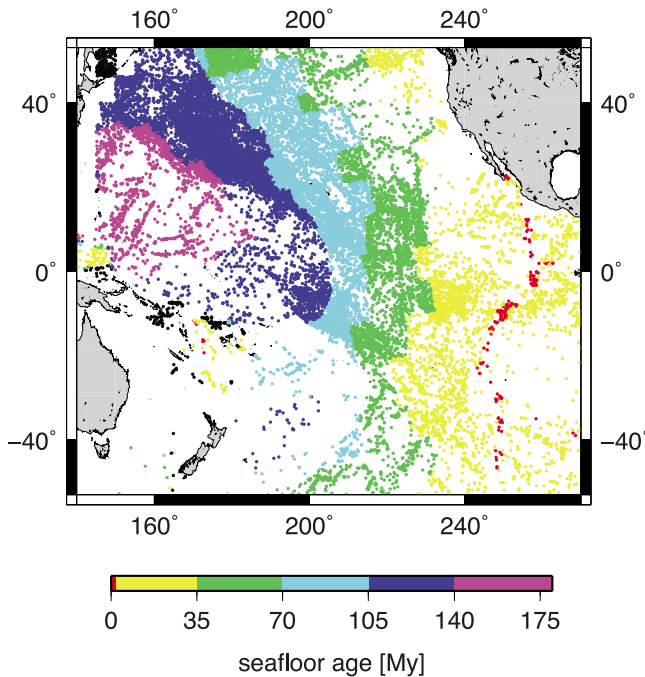


Figure 1. *SS* Pacific bouncepoints. Colored circles represent bouncepoints used in the 10° radius bins in the Pacific Ocean. Color indicates seafloor age [Müller *et al.*, 2008]. Bouncepoints on the youngest seafloor (0–2 Myr) are plotted in red to show the spreading ridges. Black bouncepoints correspond to areas without seafloor age values.

comprehensively over an oceanic plate at the resolution required to test hypotheses regarding the structure, evolution, and defining mechanism of the lithosphere.

[4] Here we use a new method to directly measure the thickness of the lithosphere over much of the Pacific plate at a resolution high enough to test hypotheses regarding the thickening of the lithosphere with respect to plate age and distance from the ridge, as well as the mechanism that defines the plates. Our method analyzes precursors to the teleseismic phase *SS*, which are sensitive to structure near the *SS* bouncepoint. Because these bouncepoints are about halfway between the sources and receivers, the observations provide a powerful tool for resolving structure in regions where seismic station coverage is sparse, such as the oceans. *SS* precursors have traditionally been used to image deeper seismic discontinuities (e.g., the mantle transition zone) [Flanagan and Shearer, 1998; Deuss and Woodhouse, 2001; Gu and Dziewonski, 2002; Houser *et al.*, 2008; Lawrence and Shearer, 2008] which produce precursor phases well separated in time from the *SS* surface reflection. However, given data of sufficient quality, shallower structures can also be resolved using *SS* precursors [Heit *et al.*, 2010; Rychert and Shearer, 2010]. We recently showed that subtle variations in the shape of stacked *SS* waveforms may be used to constrain Moho depth across Asia [Rychert and Shearer, 2010].

2. Data and Stacking Method

[5] We use the IRIS FARM data set from 1990 to 2007. We stack *SS* waveforms from epicentral distances of 90° to

140° preprocessed to remove the instrument response. We restrict source depths to 0–75 km to minimize complications from depth phases. We rotate the horizontal components to obtain the transverse component, which we then Hilbert transform to remove the expected Hilbert transform of the *SS* phase and produce more symmetric pulses. Following low-pass filtering at 0.1 Hz, we align the waveforms on the maximum amplitude (positive or negative) in a window 40 s before and 40 s after the theoretical *SS* arrival time, normalizing to unit amplitude and flipping the polarity of the negative pulses before stacking. Waveforms with peaks larger than the *SS* phase in the window 90 s preceding the phase are eliminated. We calculate the signal-to-noise ratio for each waveform using the standard deviation in a window 285 s to 60 s before the *SS* peak, and reject waveforms with signal-to-noise ratios less than 4. We obtain 310,856 waveforms that fit the source parameters described above, 95,298 of which also fit the signal-to-noise and *SS* peak criteria, and 31,417 of which have bouncepoints beneath the Pacific Ocean (Figure 1). We weight the stacked waveforms according to their signal-to-noise ratio to a maximum weight of 20 before stacking, and normalize the final stacks to unit amplitude.

3. Preliminary Stacking Results

[6] Global waveform stacks suggest first-order differences in *SS* waveform character that are likely due to lithospheric structure. For instance, the character of waveform stacks with bouncepoints beneath the Pacific is quite different than that of stacks with bouncepoints beneath continental regions (Figure 2). This difference is likely caused by the well-known large variation in the depth of the Moho, the most significant lithospheric discontinuity, between these two tectonic regions [Rychert and Shearer, 2010].

[7] Oceanic *SS* stacks are also likely influenced by a lithosphere-asthenosphere operator. This is indicated by the comparison of *SS* stacks with Pacific bouncepoints to attenuated *S* stacks of the same sources. The attenuated *S* stack fits the main pulse of the oceanic *SS* pulse, but the amplitude of its preceding side lobe fails to match that of the oceanic *SS* stack (Figure 3). This difference is likely the result of *SS* precursors reflected off a seismic discontinuity associated with the lithosphere-asthenosphere boundary; that is, a velocity decrease with depth. In addition, *SS* waveforms binned by age exhibit a progressive variation in the character of the sidelobe, which is suggestive of a lithosphere-asthenosphere boundary that increases in depth with lithospheric age (Figure 4). Here and throughout the rest of this paper we focus on the left-hand side of the *SS* waveform, since the right-hand side is significantly more variable in bootstrap realizations of the stacks.

4. Methods

[8] To investigate the structure of a discontinuity that could cause the precursor suggested by the preliminary stacks, we stack *SS* waveforms in bins with 10° radii, spaced about 10° apart, which approximate the Fresnel zone of the *SS* phase at long periods [Shearer, 1991]. We use the stacking procedures and criteria described in section 2. We model the character of the *SS* waveform using a reference

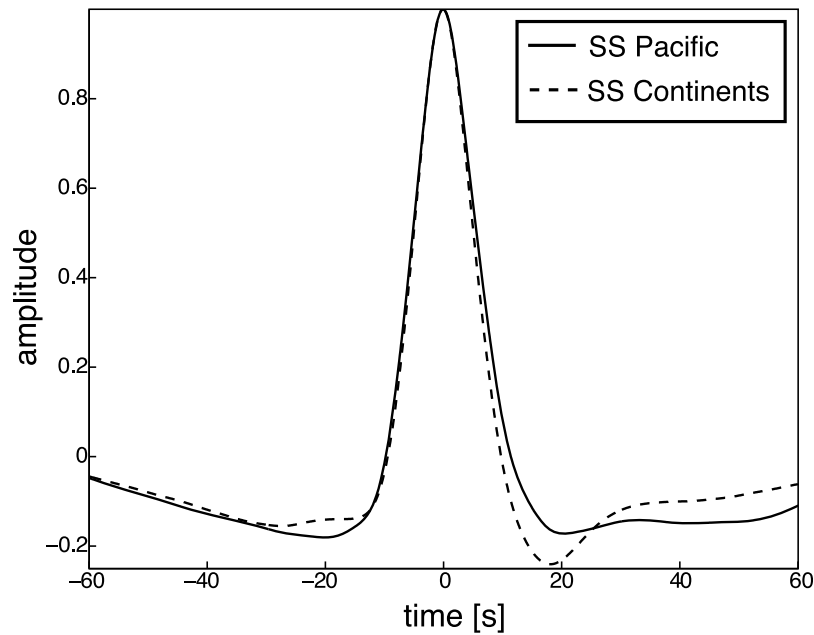


Figure 2. Pacific versus continent *SS* stack. The waveform stack of all continental *SS* bouncepoints (dashed line) determined by a tectonic regionalization model [Jordan, 1981] is compared to that of the bouncepoints in the Pacific (solid line) (Figure 1).

phase convolved with a lithospheric operator using the *SS* Lithospheric Profiling (SSLIP) method (Figure 5) [Shearer, 1996; Rychert and Shearer, 2010].

4.1. Inversion

[9] We invert the 100 s preceding the *SS* waveform peak for the best fitting lithosphere-asthenosphere seismic velocity discontinuity (velocity decrease with depth) using a

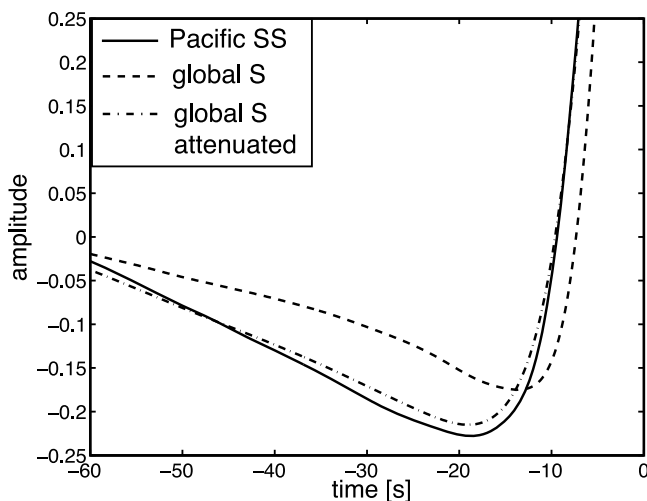


Figure 3. *S* and *SS* waveform comparison. The *S* stack (dashed line) is compared to the *SS* stack (solid line), both composed of waveforms with bouncepoints in the Pacific Ocean from bins with >500 waveforms. The reference waveform (attenuated *S* waveform with oceanic crustal operator applied) is also shown (dash-dot line). Here the maximum attenuation operator is assumed; that is, $t^* = 6$ s. Only the left-hand sidelobe of the waveforms is shown.

grid search over discontinuity depth (15–140 km), amplitude (total *S* velocity change), and sharpness (defined by the ± 1 standard deviation width of the Gaussian function we use to model a velocity gradient; i.e., twice the Gaussian half-width) (Figure 6).

4.2. Bin Selection Criteria

[10] We focus on bins with >500 *SS* waveforms [Rychert and Shearer, 2010] where a discontinuity is well resolved

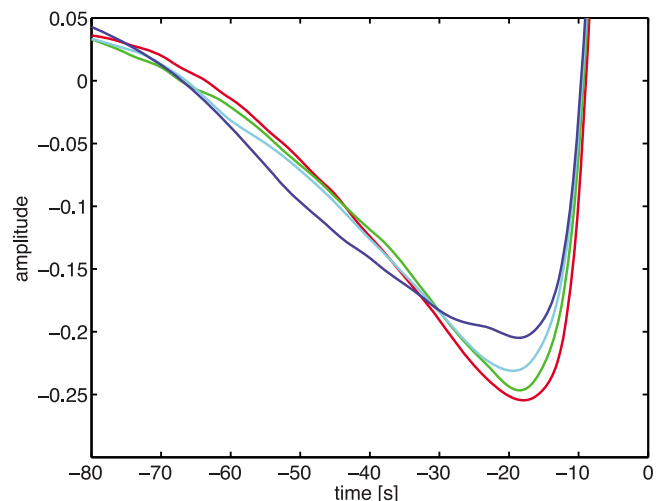


Figure 4. *SS* waveform stacked by bouncepoint in Pacific plate age bins. Only the left-hand sidelobe of the *SS* waveform is shown. Ages of bins are as follows: 0–35 Myr (red line), 35–70 Myr (green line), 70–105 Myr (cyan line), and 105–140 Myr (blue line) [Müller *et al.*, 2008]. The number of waveforms in each bin is as follows: 4204, 6098, 7380, and 11,490.

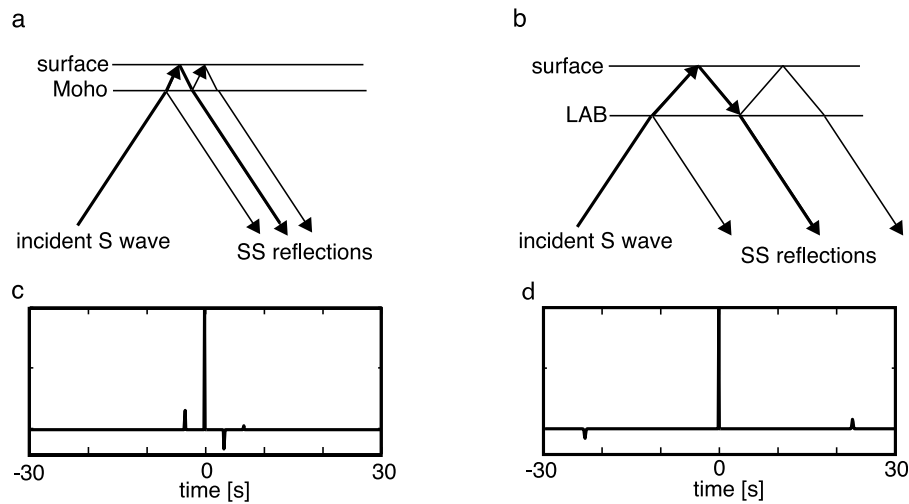


Figure 5. Schematic of raypaths and operators used in the forward model. Raypaths of the *SS* waveform (bold), the *SS* precursor (bottomside reflection), and reverberation (topside reflection) are shown for both (a) a velocity increase with depth at the Moho and (b) a velocity decrease with depth at the lithosphere-asthenosphere boundary (LAB). Examples of corresponding operators that are convolved with the reference waveform in the forward model are shown for (c) an oceanic Moho and (d) the lithosphere-asthenosphere boundary.

from the best fitting attenuated waveform, the inversion results for depth using two different *S* reference stacks (see section 4.3) are within 20 km, and the estimated error in depth to the discontinuity (see section 4.4) is <25 km using either *S* reference stack. The well-resolved bins are those in which the best fitting model fits the data significantly better than the corresponding attenuated reference phase (without a discontinuity operator), as determined by an *F* test for significance of regression [Bendat and Piersol, 2000]. The number of degrees of freedom assumed in the *F* test comparison is determined by *SS* autocorrelation; that is, assuming that the time lag of the zero crossing of the autocorrelated waveform corresponds to a degree of freedom. In the *F* test, we assume 9 degrees of freedom in the data waveforms and 4 parameters for the best fitting model compared to 1 model parameter for the attenuated waveform. These selection criteria limit our analysis to only 18 out of the original 106 bins in the Pacific Ocean. This conservative approach allows us to focus on the most reliable and well-resolved bins with good waveform fits (Figure 7). The other bins could represent areas without a discontinuity, but, given the relatively subtle effects of the feature on the waveforms, more likely represent regions of insufficient data, variability in the depth of the discontinuity, and/or complexity greater than that allowed by our model, such as multiple discontinuities. If an additional parameter is assumed in the *F* test to account for the averaging done by stacking, one additional bin is not resolved (bin 241). The results for relaxed selection criteria are briefly discussed in section 6.2.

4.3. Reference Phase

[11] The reference phase is composed of an *S* wave stack convolved with an attenuation operator to account for the additional *SS* paths through the upper mantle. The attenuation operator is allowed to vary from t^* values of 3 to 6 s in the grid search inversions [Bhattacharyya *et al.*, 1996]. We stack *S* waveforms using the same procedure and cri-

teria that we use for *SS*, but here using epicentral distances of 40° to 95° . We tried using both an *S* reference stack from all events considered (those in bouncepoint bins with >500 waveforms) and *S* reference stacks particular to each 10° bin; that is, computed from the same sources included in the corresponding *SS* stack. In both cases, signal-to-noise weighting is implemented as described for the *SS* stack. In the bin-particular case the weighting is scaled so that the total weight of each event in the *SS* stack is preserved in the *S* stack. This method was designed to eliminate possible bias from source effects that might be specific to a particular bouncepoint bin. We present inversion results using the weighted bin-specific reference stack throughout the paper, although both sets of results are very similar. One of our criteria is that the inversion results using either reference phase be within 20 km of each other (see section 4.2). An operator that approximates the oceanic crust is also included in the synthetic waveforms, although its effect on the outcome of the inversions is minimal. The crustal operator assumes a 7 km thick crust, a Moho reflection coefficient of 0.05, and a crustal shear velocity of 3.75 km/s. A test in which the SSLIP inversions were rerun using a Moho operator with 10% increases in depth and reflection coefficient resulted in best fitting SSLIP lithosphere-asthenosphere depths that were mostly unchanged, and no bins changed by more than 5 km; that is, within our error bars. The same was true for a test in which no Moho operator was included.

4.4. Error Estimation

[12] We inverted 100 bootstrap resamplings (with replacement) of the *SS* waveform stacks to determine error. Only results for bins in which the bootstrap results indicate a depth uncertainty (2σ) of less than 25 km (using a single *S* reference phase or a bin-particular *S* reference) are reported here. The distribution of error determined by bootstrap resampling is not always evenly distributed about the best

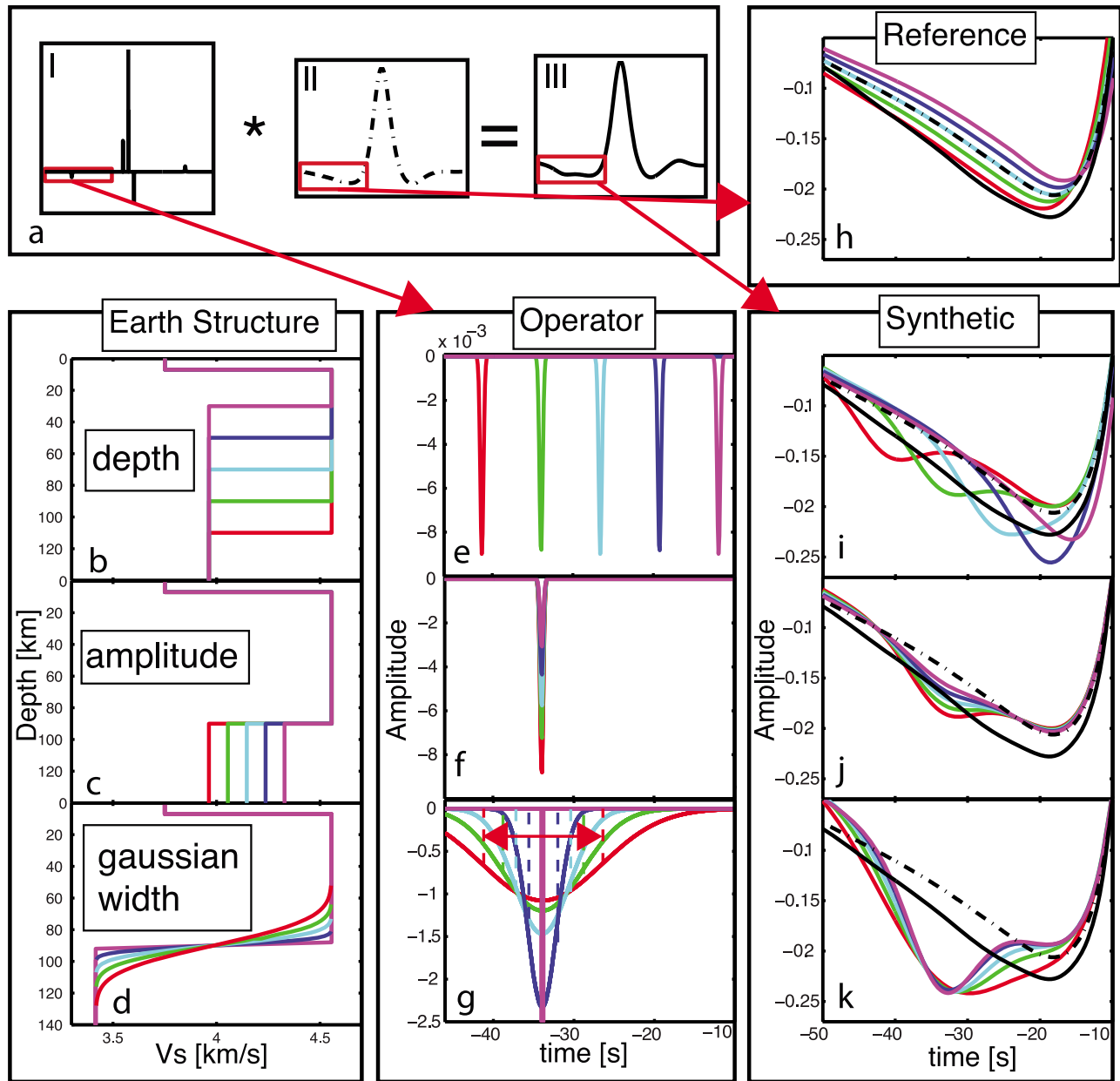


Figure 6. Parameter visualization. (a) Schematic of the forward problem, where a lithospheric operator (I) is convolved with a reference waveform (II) to produce a synthetic waveform (III). Red boxes show waveform sections that have been enlarged for visualization in Figures 6e–6k. Variations in the four model parameters are demonstrated for (b–d) Earth structure (i.e., velocity depth profiles), (e–g) lithospheric operator, (i–k) corresponding synthetic waveforms, and (h) attenuation of the reference phase. Variations in parameters are as follows: depths of 30 km (magenta line), 50 km (blue line), 70 km (cyan line), 90 km (green line), and 110 km (red line) in Figures 6b, 6e, and 6i; shear wave velocity drop of 5% (magenta line), 7% (blue line), 9% (cyan line), 11% (green line), and 13% (red line) in Figures 6c, 6f, and 6j; Gaussian widths of 0 km (magenta line), 9 km (blue line), 17 km (cyan line), 26 km (green line), and 38 km (red line) in Figures 6d, 6g, and 6k; and t^* 2.6 s (magenta line), 3.6 s (blue line), 4.6 s (cyan line), 5.6 s (green line), and 6.6 s (red line) in Figure 6h. The horizontal distance between dashed lines of like color in Figure 6g correspond to the Gaussian widths reported in this paper (twice the Gaussian half-width or ± 1 standard deviation), here shown in units of delay time. For instance, the horizontal red line with arrows shows a Gaussian width of 14.8 s, or about 38 km assuming a shear velocity of 4.36 km/s. The corresponding entire velocity drop occurs over about twice this distance in Figure 6d, ~ 76 km. The Pacific SS stack (black line) and the Pacific S stack after attenuation ($t^* = 4.6$ s) (dash-dot line) are also shown in Figures 6h–6k for comparison.

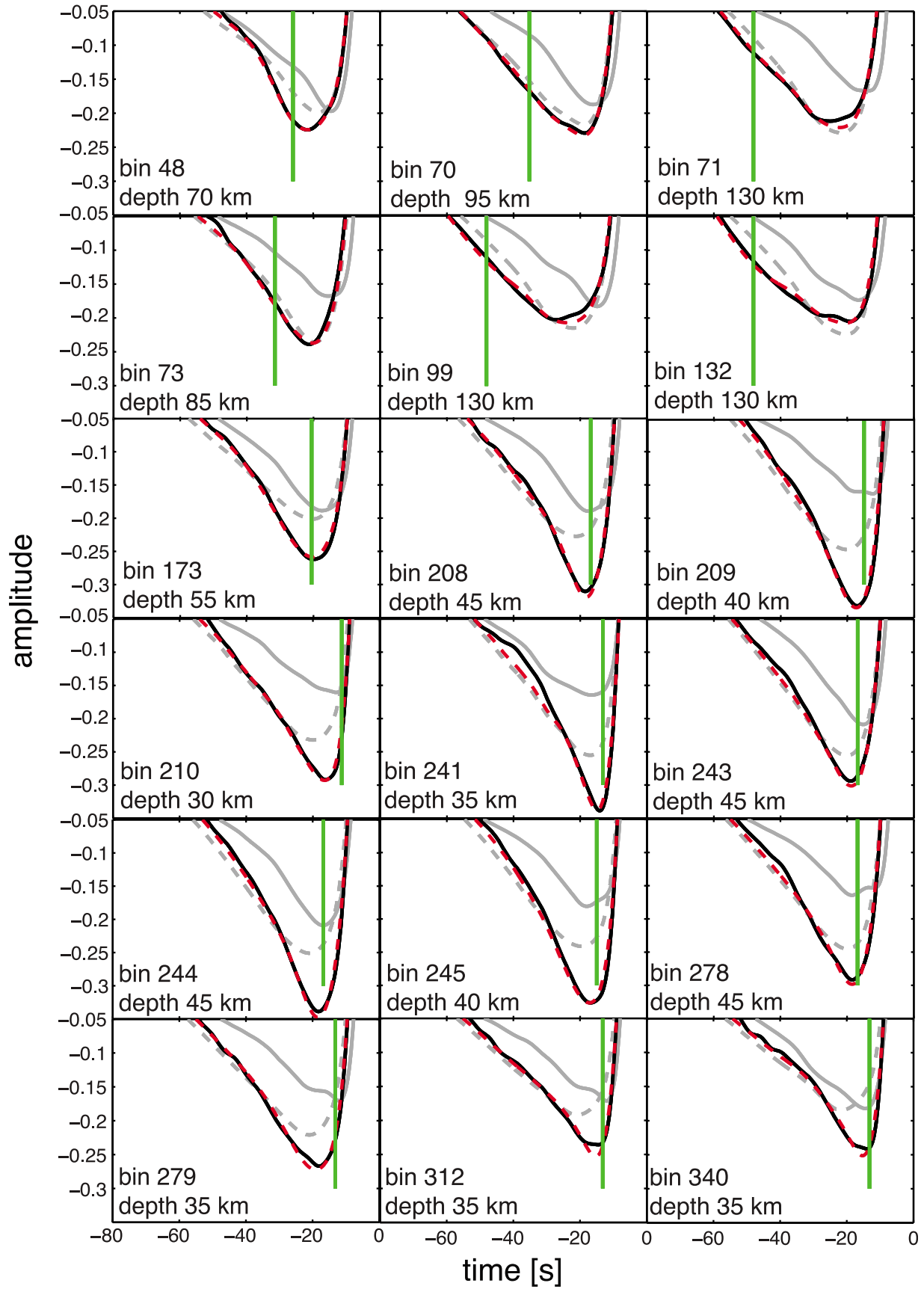


Figure 7

fitting model as reflected by the 95% confidence limits reported here.

4.5. Crustal Classification

[13] Most of the oceanic lithosphere has experienced a relatively simple tectonic history of cooling and subsidence, but processes such as hot spot alteration have affected some segments. The degree to which lithospheric thickness is affected by such phenomena is debated. However, recent results from receiver functions indicate sharp velocity drops beneath ocean island stations that are not necessarily correlated with plate age, and lithospheric thickness may be affected by thermal anomalies [Li *et al.*, 2000, 2004; Collins *et al.*, 2002; Kumar *et al.*, 2005; Vinnik *et al.*, 2005; Heit *et al.*, 2007; Rychert and Shearer, 2009; Fischer *et al.*, 2010]. Therefore, we classify our bins as normal (simple history) or anomalous (altered) on the basis of the correlation criteria model of Korenaga and Korenaga [2008]. Anomalous crust has residual bathymetry [Smith and Sandwell, 1997] with respect to the plate model of Stein and Stein [1992] that is greater than 1 km, and crust affected by anomalies is that with correlation between distance from anomalous crust and residual bathymetry < -1 m/km. We use a simplified grid in which anomalous crust and crust affected by anomalies are both considered anomalous, and the remainder of crust is considered to be normal. A spatial filter with 10° radii is applied. The bouncepoints in each bin are then classified as normal or abnormal using this filtered grid, and each 10° bin is classified as normal or abnormal on the basis of the weighted average (from the signal-to-noise ratio) of the bouncepoint classifications, with a cutoff of 50%.

5. Results

[14] We resolve a discontinuity that increases in depth with distance from the East Pacific Rise from 25 to 130 km (Figure 8). Amplitudes generally range from 4 to 13% in well-constrained bins (Table 1). Sharpnesses range from step functions to more diffuse operators that occur over depths of up to ~ 100 km (Table 1). Diffuse operators could be caused by either gradual changes in velocity with depth or variations in the depth of the discontinuity within the sensitivity region of the bin.

5.1. Depth

[15] Discontinuity depths range from 25 to 130 km. The 95% confidence limits are generally $< \pm 5$ km, and we only present bins here with error bars < 25 km. For gradual velocity gradients, discontinuity depth refers to the center of the velocity drop. Depth is scaled from the delay time of the operator assuming an upper mantle velocity of 4.556 km/s, a crustal velocity of 3.75 km/s, and a crustal thickness of 7 km. Discontinuity depths show strong correlations with a

variety of other geophysical data sets and therefore are the main focus of this paper.

5.2. Amplitude

[16] Amplitudes are calculated by convolution of the best fitting operator with the appropriate attenuated S stack to ensure frequency effects are taken into account, and scaling reflection coefficients to velocity drop assuming a velocity and density structure described in the caption of Table 1. In the majority of cases frequency effects are not significant.

[17] Amplitudes in bins with shallow discontinuity depths (≤ 40 km) are quite large ($> 13\%$). However, discontinuities in this depth range interfere strongly with the main SS pulse, and therefore SSLIP amplitude resolution is likely poor for shallow discontinuities. This may be true for discontinuities at 45 km as well. Amplitudes for bins with discontinuity depths > 40 km are generally $< 13\%$, though bins 208, 244, and 278 correspond to greater amplitudes (14–22%). The 95% confidence limits on amplitude in bins with discontinuities at depths greater than 40 km are all $< 3\%$. More precise error distributions, which reflect asymmetry about the best fitting model, are reported in Table 1.

5.3. Discontinuity Sharpness

[18] Discontinuity sharpness is reported as twice the standard deviation of the Gaussian SSLIP operator; that is, ± 1 standard deviation (twice the Gaussian half-width). Therefore the entire velocity drop occurs over a depth range that is roughly twice the reported Gaussian width. For the 10° bin results, a velocity of 4.356 km/s is assumed to translate Gaussian width from time to depth.

[19] The best fitting Gaussian widths are < 50 km, except for bins located at the greatest distances from the ridge (> 90 km $^{1/2}$). Units of km $^{1/2}$ are used to describe distance here and throughout the paper for comparison with the work of Adam and Vidal [2010]. Bins 70, 71, 99, and 132 correspond to widths of 132, 58, 79, and 58 km, respectively. Confidence limits of 95% from bootstrap realizations of the data reveal that the Gaussian widths could be even wider in some cases (Table 1).

5.4. Attenuation Correction (t^*)

[20] The attenuation operator, t^* , is allowed to vary from 3 to 6 s on the basis of a previous attenuation study using teleseismic S and SS [Bhattacharyya *et al.*, 1996]. The best fitting operator in 5 bins is the maximum value allowed, 6 s. When higher t^* values are allowed, only two bins are better fit by a higher attenuation operator. Bin 173 and bin 208 are better fit by operators of 6.5 and 6.25 s, respectively. However, amplitude and sharpness are unchanged, and the depth to the discontinuity is only minimally changed, decreased by 5 km in bin 173 and increased by 5 km in bin 208.

Figure 7. Waveform fits for 10° bins for inversions using bin-specific reference S wave stacks. The solid gray line shows the original S stack for the bin. The dashed gray line shows the attenuated S stack with the best fitting attenuation operator. The black line shows the SS stack (data). The dashed red line shows the best fitting synthetic waveform; that is, the attenuated S stack convolved with a lithospheric operator. The vertical green line corresponds to the delay time of the best fitting lithospheric operator, which is used to compute the discontinuity depths indicated. The global bin numbers and the best fitting depths (in kilometers) are shown in the lower left-hand corners. Only bins with > 500 waveforms, where inversion results are well resolved from the attenuated S reference stack, are in agreement (within 20 km) using two different reference phases and with standard deviation in depth to the discontinuity < 25 km using either reference phase, are shown.

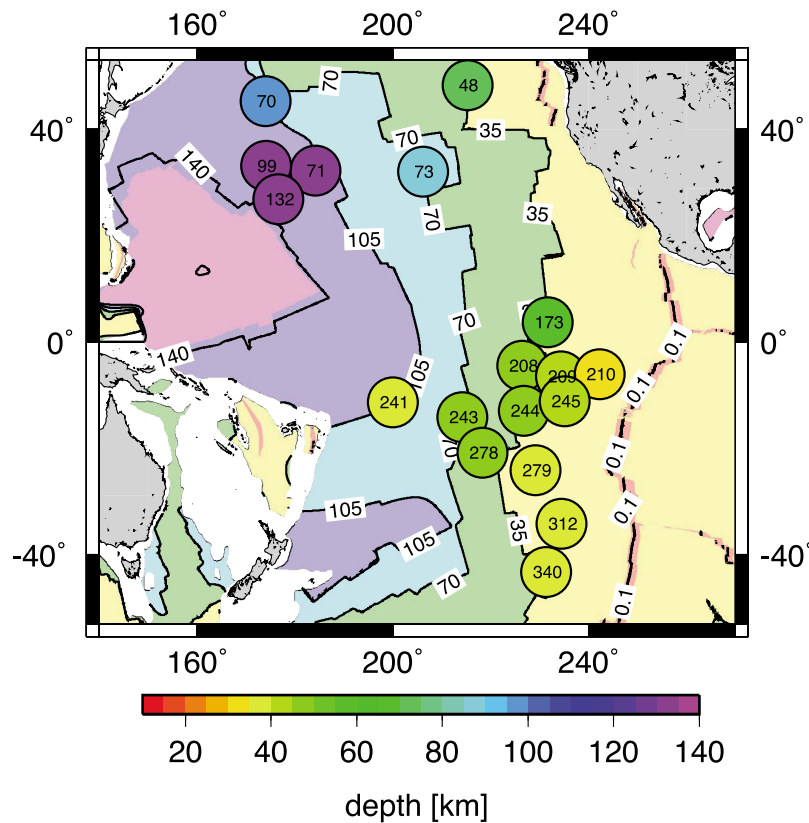


Figure 8. Pacific bouncepoint caps with well-resolved lithosphere-asthenosphere depths. Circle colors correspond to the depth of the discontinuity from the SSLIP inversion result. Only bins with >500 waveforms, a well-resolved discontinuity, small error (<25 km), and depth agreement (within 20 km) between inversions using two different reference phases are shown. These are the results of inversion for the best fitting four parameters using a bin-particular reference S phase. Background pastel colors show seafloor age from young (0–35 Myr in yellow) to old (140–175 Myr in magenta) [Müller *et al.*, 2008]. Numbers within the circles represent global bin numbers and correspond to the bin numbers in Table 1. Depth is in relation to the seafloor.

5.5. Parameter Relationships

[21] Overall the parameters are not strongly correlated with one another. Depth and amplitude are negatively correlated (correlation coefficient -0.70), since amplitude is negatively correlated with the square root of distance from the ridge (correlation coefficient -0.73). However, amplitude may not be well resolved at small distances where the discontinuity operator interferes with the main SS pulse. In addition, although Gaussian width is not strongly correlated with other parameters, Gaussian widths at large distances from the ridge are larger than those of the other bins. However, Gaussian width could either represent a gradual velocity gradient in depth or a discontinuity that varies in depth over the sensitivity region of the bin. Therefore the tectonic significance of this variation is uncertain. We do not observe strong correlations between t^* and any other parameters.

6. Discussion

[22] SSLIP resolves a velocity drop that increases in depth with respect to seafloor age and/or distance from the ridge, in general agreement with the notion of an oceanic plate that increases in thickness as it ages and moves away from the ridge as indicated by gravity, heat flow, depth of seismicity,

and seismic imaging [Parsons and Sclater, 1977; Watts, 1978; Nishimura and Forsyth, 1989; Stein and Stein, 1992]. The large lateral extent of the observed velocity drop combined with its depth-distance trend suggests that it is likely the lithosphere-asthenosphere boundary.

6.1. Distance Along Flow Line and Square Root of Age

[23] The depth of the SSLIP discontinuity is correlated with the square root of distance from the ridge along flow lines [Adam and Vidal, 2010] (Figure 9). The correlation coefficient is 0.96 for bins located on normal crust (see section 4.5) and 0.89 for all bins. The thermal contour with the best fit to the SSLIP depths from normal oceanic crust is 930°C with 95% confidence limits $820\text{--}1020^\circ\text{C}$ (Figure 9).

[24] Here distance is calculated using a weighted average of the age of each bouncepoint included in the bin, which is determined by a spatially filtered grid from NUVEL1. Thermal contours assume half-space cooling with potential temperature = 1350°C , thermal diffusivity = 10^{-6} mm²/s, and plate velocity = 60 km/Myr. Assuming an average plate velocity 10 km/Myr faster increases the best fitting thermal contour by 50°C . If bins on both normal and anomalous crust are included, the best fitting thermal contour is

Table 1. Results for Individual *SS* Bouncepoint Bins^a

Bin	Type	Age (Myr ^{1/2})	Distance (km ^{1/2})	SSLIP Depth (km)	Depth Bounds (km)	Amplitude (%)	Amplitude Bounds (%)	Sharpness (km)	Sharpness Bounds (km)	<i>t</i> [*] (s)	<i>t</i> [*] Bounds (s)
48	N	6.2	64.0	70	60–74	11	6–16	26	2–48	3.75	3.3–4.4
70	A	9.9	95.4	95	86–128	4	3–7	132	108–170	5.5	5.0–6.0
71	A	10.3	90.7	130	130–140	7	6–11	58	55–77	5.75	5.3–6.0
73	N	8.7	74.9	85	69–93	5	3–11	17	2–34	4.75	4.5–5.4
99	A	11.0	96.4	130	130–130	11	7–11	79	62–89	5.25	5.0–5.5
132	A	11.3	94.8	130	120–130	12	7–12	58	34–65	5.75	5.5–6.0
173	N	5.6	50.9	55	50–59	13	11–18	42	18–48	6	5.8–6.0
208	N	6.3	49.8	45	40–50	22	17–24	9	2–28	6	5.8–6.0
209	N	5.2	40.8	40	35–46	(20)	17–25	21	10–25	5.5	4.8–5.7
210	N	3.8	30.0	30	25–39	(18)	16–22	29	2–36	4.75	4.3–5.4
241	A	10.3	72.8	35	30–40	(20)	17–22	0	0–17	3.5	3.0–4.0
243	A	8.0	59.9	45	40–50	12	10–14	9	0–17	5.5	5.5–6.0
244	N	5.9	47.3	45	40–45	22	19–25	13	6–32	6	5.7–6.0
245	N	4.9	37.8	40	30–44	(18)	18–22	34	10–36	4.75	4.3–5.2
278	A	6.8	55.8	45	40–54	14	10–16	5	0–28	6	5.5–6.0
279	N	5.2	43.8	35	30–63	(13)	6–18	46	28–87	6	5.3–6.0
312	N	4.8	34.8	35	30–39	(19)	12–21	5	0–32	4.5	4.0–5.2
340	N	5.4	32.0	35	30–39	(21)	17–26	9	0–24	4.25	3.5–5.0
PA06 (SW)	NA	7.6–11.2	61.8–79.6	46	27–50	7	3–10	0	0–34	5	4.8–5.5
PA5	A	9.3–11.7	70.7–86.9	48	33–52	7	3–10	28	0–47	4.5	4.0–5.2

^aBounds represent 95% confidence limits from bootstrap inversions. Assumptions for time-depth and reflection coefficient-amplitude (percent) scalings include the following: crustal $V_s = 3.75$ km/s, mantle $V_s = 4.556$ km/s, crustal thickness = 7 km, and mantle density = 3.38 g/cm³. Time-depth scaling for the sharpness of the discontinuity assumes a velocity of $V_s = 4.356$ km/s; that is, approximately the velocity at the middle of the gradient between lithosphere and asthenosphere. Depth is in relation to the seafloor. Amplitude refers to the shear wave velocity drop (percent) in depth. PA06 and PA5 correspond to SSLIP inversions for regions approximating the sensitivities of two previous studies, PA06 [Tan and Helmlberger, 2007] and PA5 [Gaherty *et al.*, 1999]. For comparison to PA06 and PA5 the crust and lid Voigt averages reported by those studies are used, and the mantle density is assumed to be constant, 3.38 g/cm³. If a decrease in density with depth is also assumed, as in model PA5 from 3.38 to 3.35 g/cm³, the SSLIP velocity drop is decreased by $\sim 1\%$. Bins marked “N” represent predominantly normal crust, those marked “A” represent crust that is anomalous or near to anomalous crust, and those marked “NA” represent bins that sample normal and abnormal crust in roughly equal proportions [Korenaga and Korenaga, 2008]. Amplitudes for bins with discontinuity depths ≤ 40 km may be poorly resolved owing to interference with the main *SS* pulse and are reported in parentheses. Amplitudes of discontinuities at 45 km depth may also be slightly influenced by this effect.

increased by $\sim 30^\circ\text{C}$ to 960°C with 95% confidence limits 740–1120°C.

[25] The thermal contour that best fits our model (930°C) is slightly greater than that of the brittle ductile transition based on the maximum depth of seismicity, $\sim 600^\circ\text{C}$ [Abercrombie and Ekström, 2001] and also the isotherm associated with the effective elastic thickness of the plate at 450–700°C [Watts, 1978; Kuo *et al.*, 1986]. The small number of reliable bins that are also anomalous prevents us from definitely determining whether the thickness of anomalous oceanic lithosphere is any different than normal lithosphere in terms of its relationship to the square root of distance from the ridge along mantle flow lines.

[26] Our results also show an increase in depth to the discontinuity with seafloor age, although there is more scatter in this comparison (Figure 10). Age is calculated from a weighted average of the age of each bouncepoint included in the bin, which is determined by a spatially filtered grid from the model of Müller *et al.* [2008]; that is, exactly the same way that distance is calculated. Assuming that the plate model and the square root distance model fit subsidence/bathymetry roughly equally well, and that SSLIP follows a similar pattern, this variation in SSLIP fit is not necessarily expected. However, the data fit by the Stein and Stein [1992] plate model were primarily from the North Pacific and northwest Atlantic; that is, not the region of our best-resolved bins. Comparisons of age and distance to bathymetry (averaged the same way) in the sensitivity regions of our best bins show similar complexity, with age versus bathymetry showing slightly more scatter than dis-

tance versus bathymetry. Therefore, this complexity is likely real. For simplicity, we interpret our results in terms of distance from the ridge along flow lines for the remainder of the paper, although in most cases distance could be replaced by age as a descriptor.

6.2. Relaxation of Selection Criteria

[27] If the bin selection criteria are relaxed; that is, if we consider all 45 bins with >500 waveforms, regardless of whether or not the discontinuity is well resolved, we find a very similar pattern to that found with just the best bins, plus an additional population of bins numbering ~ 17 that suggest a discontinuity at constant depth, ~ 40 km depth. The bins with shallow discontinuities at constant depth are mostly (13 of the 17) coincident or adjacent to the sensitivity region of two previous studies of Pacific transects which also found a constant depth discontinuity [Gaherty *et al.*, 1999; Tan and Helmlberger, 2007] (Figure 11). Discontinuity depth is not resolved in these bins, possibly because multiple discontinuities exist in depth, which are not resolvable with our method given the subtlety of the feature we are matching. Therefore, we focus on those bins that are well resolved.

6.3. Comparison to Previous Studies

[28] Our results are in general agreement with lithospheric thickening with distance from the ridge observed by surface-wave models. Surface waves resolve gradual decreases in velocity with depth. Thus, there is some ambiguity regarding the exact depth of the lithosphere-asthenosphere boundary in these models. However, the depth to the

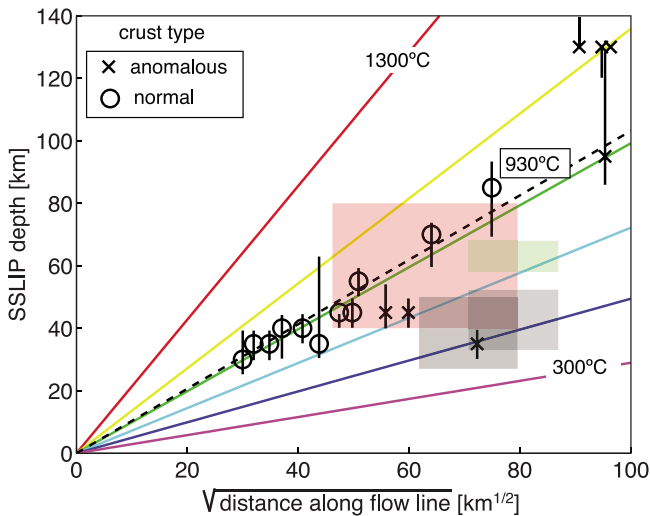


Figure 9. SSLIP depth versus distance from ridge along flow line and comparison to previous studies. Open circles correspond to bins located on predominantly normal oceanic crust. Crosses correspond to bins that are located on crust that is anomalous, or altered in some way as described in the text after *Korenaga and Korenaga* [2008]. Black vertical lines indicate 95% confidence limits. Colored lines show a half-space cooling model assuming a potential temperature of 1350°C and a plate velocity of 60 mm/yr for thermal contours from 300°C (magenta line) to 1300°C (red line) at 200°C intervals. The dashed black line shows the best fitting thermal contour (930°C) from a weighted least squares inversion of the SSLIP inversion results from bins on predominantly normal crust. Colored boxes show results from previous studies by *Tan and Helmlberger* [2007] (red) and *Gaherty et al.* [1999] (green). Gray boxes show SSLIP results from the approximate regions of the southwest portion of the *Tan and Helmlberger* [2007] transect and the *Gaherty et al.* [1999] transect. The result from *Kawakatsu et al.* [2009] is not shown here since it is not located on the Pacific plate and therefore corresponds to different flow lines. Depth is in relation to the seafloor.

boundary is very similar to lateral variations in global surface-wave velocity models. For example, our result is correlated with Voigt-averaged shear velocities at 100 km depth, with a correlation coefficient of 0.85 for normal crust and 0.89 for all crust in a global surface-wave model (Figure 12) [*Nettles and Dziewonski*, 2008]. Our results are not likely related to the anisotropic boundary that exists at ~80 km depth across the ocean in surface-wave models [*Ekström and Dziewonski*, 1998; *Gung et al.*, 2003; *Nettles and Dziewonski*, 2008] since our results are relatively insensitive to purely anisotropic discontinuities.

[29] To compare with previous studies of Pacific transects [*Gaherty et al.*, 1999; *Tan and Helmlberger*, 2007] we stacked *SS* waveforms with bouncepoints approximating their sensitivity regions (Figure 11). We inverted for discontinuity structure using reference *S* phases composed of the sources in the corresponding *SS* stacks; that is, the same method used for the 10° bin inversion (Figure 13). The SSLIP method does not find a resolvable discontinuity in areas that approximate either study region using the criteria

for resolution described for the 10° bin inversions. This could be owing to the lack of a discontinuity, although it is more likely due to variations in discontinuity depth over the sensitivity region and/or discontinuity structure that is more complex than that allowed by our model. We have tested more complicated models, for example a sharp drop in velocity underlain by a more gradual velocity drop, to approximate the 1-D models reported by [*Gaherty et al.*, 1999; *Tan and Helmlberger*, 2007], but more complicated structure is similarly difficult to resolve given the relatively subtle nature of the feature that we are trying to match. We also tried splitting the transect approximating the *Tan and Helmlberger* [2007] study region in half to focus on smaller regions (see Figure 11). However, the discontinuity was similarly unresolved in either of the half-transects. Similarly, SSLIP inversions of the 10° bins with >500 waveforms within the sensitivity regions of these studies do not find a resolvable discontinuity (Figure 11).

[30] Discontinuity structure that is not resolved within our uncertainty limits does not necessarily indicate the lack of a discontinuity, since more complex structure could also be the explanation. Therefore we compare our results to previous studies of Pacific transects. The best fitting SSLIP discontinuities in this region (27–50 km and 33–52 km depth) broadly agree with the depth of the sharp drop reported by one study (40–80 km) [*Tan and Helmlberger*, 2007]

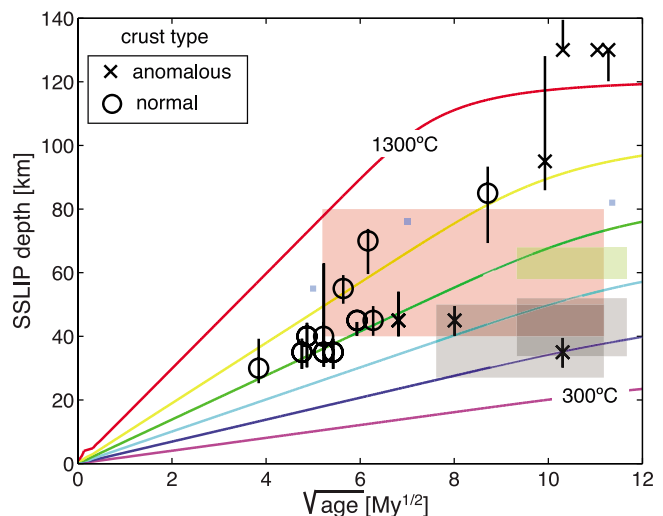


Figure 10. SSLIP depth versus square root of age. SSLIP results from normal crust (circles) and anomalous crust (crosses) are compared to the square root of age. Colored lines show the plate model [*Stein and Stein*, 1992] assuming a potential temperature of 1350°C and a plate velocity of 60 mm/yr for 200°C thermal contours from 300°C (magenta) to 1300°C (red). Colored boxes show results from previous studies by *Tan and Helmlberger* [2007] (red), *Gaherty et al.* [1999] (green), and *Kawakatsu et al.* [2009] (small blue boxes). Gray boxes show SSLIP results from the approximate regions of the southwest portion of the *Tan and Helmlberger* [2007] and *Gaherty et al.* [1999] transects. Age is calculated from a weighted average of the age of each included in the bin, which is determined by a spatially filtered grid from the model of *Müller et al.* [2008]. Depth is in relation to the seafloor.

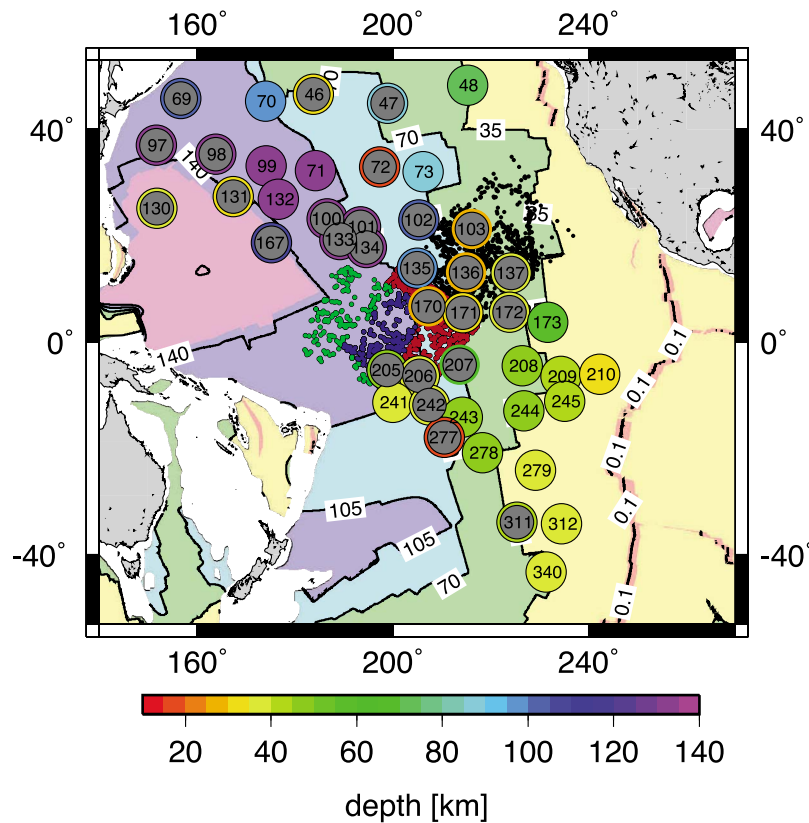


Figure 11. Pacific bouncepoint caps with >500 waveforms and bouncepoints that approximate regions studied in two previous publications. Large colored circles show the depth of the discontinuity from the SSLIP inversion result. Bins that do not meet the selection criteria of the best bins are overprinted with a slightly smaller gray circle. Small green and blue dots show bouncepoints approximating the study region of *Gaherty et al.* [1999]. Small red and blue dots show bouncepoints approximating the southwestern portion of the study region of *Tan and Helmberger* [2007]. Small black dots represent the northeastern portion of the *Tan and Helmberger* [2007] transect, which is not included in the SSLIP modeling shown here, as described in section 6.3. Background pastel colors show seafloor age from young (0–35 Myr in pink) to old (140–175 Myr in blue) [*Müller et al.*, 2008]. Numbers within circles represent global bin numbers. Depth is in relation to the seafloor.

and are just shallower than that of the other (58–68 km) [*Gaherty et al.*, 1999] (see Figures 9, 10, and 14). Depths reported here are with respect to the seafloor, rather than the sea surface. The shape of the velocity gradient also agrees: a 3–10% change over <35 and <50 km depth versus a sharp ~6% drop [*Gaherty et al.*, 1999; *Tan and Helmberger*, 2007]. This overall agreement of our best fitting models verifies our method for imaging velocity discontinuities beneath the Pacific, although greater complexity is suggested.

[31] Results from these former studies are also in agreement with the thermal contour defining the lithosphere-asthenosphere boundary as defined by the SSLIP results (green and red boxes compared to the dashed black line in Figure 9). The SSLIP inversion results from regions approximating these studies (gray boxes in Figure 9) are just shallower than the best fitting range of thermal contours (740–1120°C). SSLIP results are also generally in agreement with lithosphere-asthenosphere boundary depths from converted phases when compared in terms of age (small blue boxes in Figure 10) [*Kawakatsu et al.*, 2009].

[32] Our *SS* precursor results are in broad agreement with surface-wave, converted-phase, and ScS and multiple *S* bounce models for the Pacific as described in the previous paragraphs. However, the surface-wave and the converted-phase models suggest a lithosphere-asthenosphere boundary that increases in depth with distance/age, while ScS and multiple *S* bounce models support a constant depth discontinuity. More complex structures may be required to reconcile the two models.

[33] The numerous SSLIP results that correlate to square root of distance along flow lines at small distances (<60 km^{1/2}) may represent the thermal boundary layer before the boundary at constant depth is formed. In other words, if the constant depth boundary, sometimes referred to as the Gutenberg discontinuity [*Gutenberg*, 1948] or G [*Gaherty et al.*, 1999] represents a compositional boundary related to the melt separation zone [*Gaherty et al.*, 1999], it would only be expected in thicker lithosphere; that is, at distances greater than about 60 km^{1/2} in our models (Figure 9). It has been suggested that G might extend back to the ridge beneath the lithosphere [*Gaherty et al.*, 1999], and a constant depth high-conductivity layer has been observed near

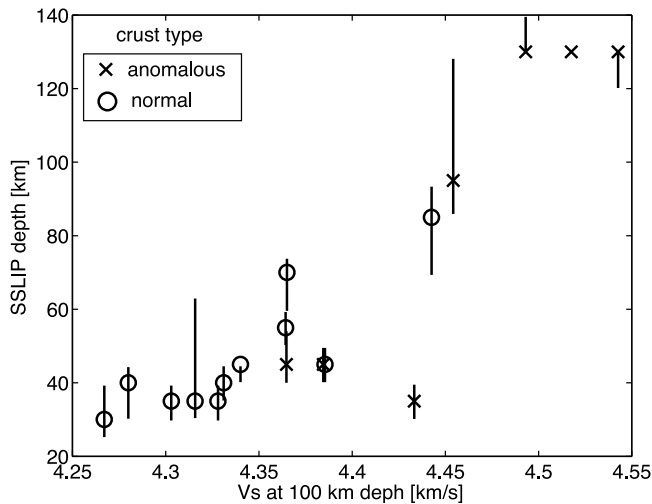


Figure 12. SSLIP depth versus V_s (Voigt average) at 100 km in the model of *Nettles and Dziewoński* [2008]. Open circles correspond to bins located on predominantly normal oceanic crust. Crosses correspond to bins that are located on crust that is anomalous, or altered in some way as described in the section 4.5 using the model of *Korenaga and Korenaga* [2008]. Black vertical lines represent 95% confidence limits from a bootstrap resampling method. Depth is in relation to the seafloor.

the East Pacific Rise [*Evans et al.*, 2005; *Baba et al.*, 2006]. However, we do not observe evidence of a G discontinuity from 0 to 60 km^{1/2}, which is consistent with isotropic surface-wave models near the ridge [*Harmon et al.*, 2009].

[34] At distances greater than 60 km^{1/2} a sharp compositional velocity drop, underlain by a more gradual drop as in the models reported by [*Gaherty et al.*, 1999; *Tan and Helmberger*, 2007] may exist. In this case the deeper gradual drop is likely a thermal boundary layer. However, this more complicated 1-D structure is not resolvable with

SSLIP. Indeed, from 60 to 90 km^{1/2} there are only three well-resolved SSLIP bins, bins 48, 73, and 241 (Figure 9). Bin 241 is at the edge of being significantly resolved, but is quite shallow and more consistent with a constant depth boundary. Overall complicated 1-D discontinuity structure at distances of 60–90 km^{1/2} could be the reason that SSLIP resolves discontinuities in so few bins in this distance range. An alternative explanation is lateral variations in the depth to the discontinuity within the 10° bins.

[35] SSLIP discontinuities at distances >90 km^{1/2} are generally deep. These bins are all located on anomalous crust, and therefore alteration could be the reason that they do not evidence a strong discontinuity at 60 km depth. Alternatively, G may be absent at great distances >90 km^{1/2} owing to a decrease in the impact of water on olivine rheology and mantle shear velocity as temperatures cool [*Faul and Jackson*, 2005; *Fischer et al.*, 2010]. Lithosphere-asthenosphere boundary depths consistent with lithospheric thickening with age for old oceanic lithosphere rather than a pronounced G discontinuity has also been suggested using converted phases beneath the Pacific Plate [*Kawakatsu et al.*, 2009].

6.4. Discontinuity Sharpness, Strength, and Shallowness

[36] The best fitting discontinuity is quite sharp (i.e., a relatively large velocity change over a small Gaussian width) in many bins that are close to the ridge (<90 km^{1/2}). For example, bins 312 and 340 correspond to Gaussian widths of 5 to 9 km for the best fitting model, corresponding to velocity drops that occur over a total depth range of about 10–18 km. Such gradients are sharper than expected for a conductively cooling lid, even when grain size evolution is accounted for, which occur over depths of >50 km for most plate ages [*Austin and Evans*, 2007; *Behn et al.*, 2009].

[37] Bins in which the best fitting model corresponds to a gradual discontinuity in depth are consistent with a boundary that is defined by temperature or temperature and grain size

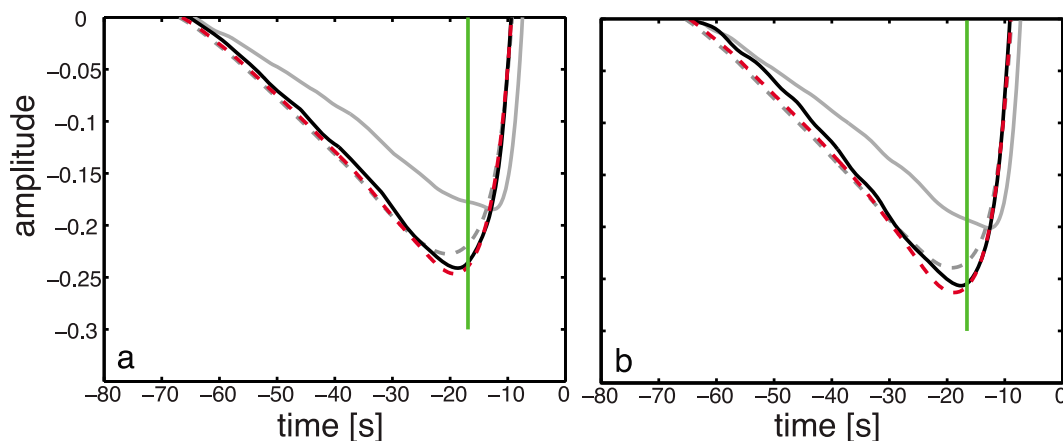


Figure 13. SSLIP waveform fits for regions corresponding to previously published velocity models (a) PAC06 [*Tan and Helmberger*, 2007] (southwest portion) and (b) PA5 [*Gaherty et al.*, 1999]. Black lines show SS data stacks for bouncepoint regions approximating locations of previous publications. Solid gray lines show the bin particular S wave stacks. Dashed gray lines show the reference S wave stacks attenuated using the best fitting t^* operator, 5 and 4.5 s. Dashed red lines show the best fitting SSLIP waveform from the inversion. Green lines show the locations of the lithospheric operators.

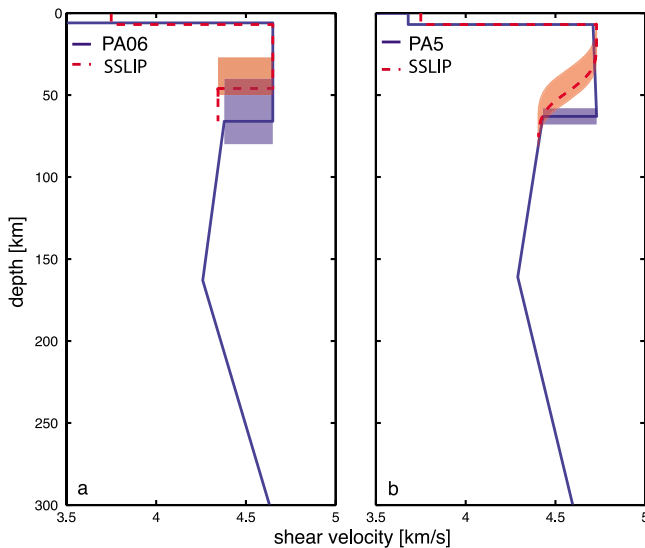


Figure 14. SSLIP inversion results (dashed red lines) compared to published velocity models for the Pacific (blue lines) for (a) PAC06 [Tan and Helmberger, 2007] (south-west portion) and (b) PA5 [Gaherty et al., 1999]. Translucent blocks correspond to estimated errors in the depth of the base of the lid as reported by the previous studies (blue box) and from SSLIP (red box). Depth is in relation to the seafloor.

[Faul and Jackson, 2005; Stixrude and Lithgow-Bertelloni, 2005; Priestley and McKenzie, 2006]. However, bins best fit by gradual velocity drops do not preclude the possibility of sharp discontinuity structure, since variations in the depth of the discontinuity may occur within the sensitivity region of the bin rather than gradual velocity drops in depth.

[38] The strength of the velocity drop is also large, 4–13% in bins where the amplitude is well resolved. Surface-wave velocity drops agree with the lower end of the SSLIP amplitudes, ~3–5% [Nettles and Dzierwoński, 2008]. However, larger velocity variations may not be resolvable by surface waves given the lower depth resolution. Studies using ScS and multiple bounce S waves find total drops of 9–11% [Gaherty et al., 1999; Tan and Helmberger, 2007] or even up to 14.3% [Bagley and Revenaugh, 2008] in agreement with the upper end of the amplitudes in well-resolved bins.

[39] Considering both the magnitude and sharpness of the velocity drop, several bins in the southern Pacific correspond to velocity drops that are too sharp to be explained thermally, $\geq 0.9\%/km$ (bins 208, 241, 243, 244, 278, 312, 340), certainly sharper than expected from conductive cooling and grain size variations, which are on the order of $\sim 0.2\%/km$ [Behn et al., 2009]. Amplitudes for some of these bins may be poorly constrained and unrealistically large, especially those $>13\%$, and 95% confidence limits indicate that Gaussian widths could be wider in some cases. Better SSLIP amplitude and sharpness constraints will be necessary for closer investigation of the mechanism that defines our observations. However, the strength and sharpness of some bins close to the ridge suggest that an additional mechanism besides temperature may also be required to explain the observations [Rychert et al., 2005, 2007, 2010; Fischer et al., 2010].

[40] Other mechanisms that have been proposed to explain strong, sharp contrasts include hydration [Hirth and Kohlstedt, 1996; Karato, 2003; Dalton et al., 2009; Karato, 2010] or melting [Anderson and Sammis, 1970; Takei, 2002; Holtzman et al., 2003; Hirano et al., 2006; Mierdel et al., 2007; Tan and Helmberger, 2007; Kawakatsu et al., 2009; Kohlstedt and Holtzman, 2009; Takei and Holtzman, 2009; Hirschmann, 2010] in the asthenosphere. Hydration alone may not explain the large (4–13%) observed velocity contrasts, especially at colder temperatures where the effect of hydrated olivine on seismic waves is decreased [Behn et al., 2009]. Similarly, half-space cooling models of a dry mantle do not predict melting along the 930°C isotherm, and suggest that melting may be more likely at greater depths, where the mantle is at its potential temperature $\sim 1350^\circ C$. Assuming an average plate velocity 10 km/Myr faster increases the best fitting thermal contour by 50°C and including bins on both normal and anomalous crust in the fit increases the contour by an additional $\sim 30^\circ C$. However, the depth/temperature range is still shallower than where temperatures reach the maximum. One possibility is that the lithosphere-asthenosphere boundary may represent a permeability boundary [Sparks and Parmentier, 1991; Hirschmann, 2010; Katz, 2010]. Hydrous melt rises to the boundary and ponds, hydration is accumulated on the boundary, and a small degree of partial melting is maintained at the boundary. In this case the lithosphere-asthenosphere boundary represents the wet solidus.

7. Conclusions

[41] The SSLIP method for analysis of SS waveforms resolves a significant velocity drop at depths of 25 to 130 km depth beneath much of the Pacific. The large lateral extent of the observed velocity drop combined with its depth-distance trend suggests that it is likely the lithosphere-asthenosphere boundary. Correlation of the depth of the boundary with the square root of distance from the ridge suggests that the depth of the oceanic lithosphere-asthenosphere boundary is regulated by conductive cooling along mantle flow lines, and the thickness of the Pacific plate corresponds to an isotherm at 930°C with a 95% confidence region of 820–1020°C. The sharpness of the discontinuity suggests that a mechanism besides a thermal gradient, such as water or melting in the asthenosphere may be necessary to define the boundary even if its depth is controlled thermally. One possibility is that the imaged interface represents a permeability boundary, with a small amount of partial melting below it. Although the results presented here are for only a portion of the Pacific, given sufficient data the SSLIP method has the potential to eventually map the lithosphere-asthenosphere boundary over entire ocean basins, which should permit a more detailed understanding of the thermal and tectonic evolution of the oceanic plates.

[42] **Acknowledgments.** We thank Jim Gaherty, one anonymous reviewer, and the Associate Editor for helpful reviews. This work also benefited from discussions with Nicholas Harmon, Terry Plank, Marc Parmentier, Greg Hirth, and Richard Katz. This research was supported in part by National Science Foundation grant EAR-0710881 and a Natural Environment Research Council fellowship.

References

- Abercrombie, R. E., and G. Ekström (2001), Earthquake slip on oceanic transform faults, *Nature*, *410*, 74–77, doi:10.1038/35065064.
- Adam, C., and V. Vidal (2010), Mantle flow drives the subsidence of oceanic plates, *Science*, *328*, 83–85, doi:10.1126/science.1185906.
- Anderson, D., and C. Sammis (1970), Partial melting in the upper mantle, *Phys. Earth Planet. Inter.*, *3*, 41–50, doi:10.1016/0031-9201(70)90042-7.
- Austin, N., and R. Evans (2007), Paleowattmeters: A scaling relation for dynamically recrystallized grain size, *Geology*, *35*, 343–346, doi:10.1130/G23244A.1.
- Baba, K., A. D. Chave, R. L. Evans, G. Hirth, and R. L. Mackie (2006), Mantle dynamics beneath the East Pacific Rise at 17°S: Insights from the Mantle Electromagnetic and Tomography (MELT) experiment, *J. Geophys. Res.*, *111*, B02101, doi:10.1029/2004JB003598.
- Bagley, B., and J. Revenaugh (2008), Upper mantle seismic shear discontinuities of the Pacific, *J. Geophys. Res.*, *113*, B12301, doi:10.1029/2008JB005692.
- Behn, M. D., G. Hirth, and J. R. Elsenbeck (2009), Implications of grain size evolution on the seismic structure of the oceanic upper mantle, *Earth Planet. Sci. Lett.*, *282*, 178–189, doi:10.1016/j.epsl.2009.03.014.
- Bendat, J., and A. Piersol (2000), *Random Data Analysis and Measurement Procedures*, 3rd ed., 594 pp., John Wiley, New York.
- Bhattacharyya, J., G. Masters, and P. Shearer (1996), Global lateral variations of shear wave attenuation in the upper mantle, *J. Geophys. Res.*, *101*, 22,273–22,289, doi:10.1029/96JB01782.
- Collins, J. A., F. L. Vernon, J. A. Orcutt, and R. A. Stephen (2002), Upper mantle structure beneath the Hawaiian swell: Constraints from the ocean seismic network pilot experiment, *Geophys. Res. Lett.*, *29*(11), 1522, doi:10.1029/2001GL013302.
- Dalton, C. A., G. Ekström, and A. M. Dziewonski (2009), Global seismological shear velocity and attenuation: A comparison with experimental observations, *Earth Planet. Sci. Lett.*, *284*, 65–75, doi:10.1016/j.epsl.2009.04.009.
- Deuss, A., and J. Woodhouse (2001), Seismic observations of splitting of the mid-transition zone discontinuity in Earth's mantle, *Science*, *294*, 354–357, doi:10.1126/science.1063524.
- Ekström, G., and A. M. Dziewonski (1998), The unique anisotropy of the Pacific upper mantle, *Nature*, *394*, 168–172, doi:10.1038/28148.
- Evans, R. L., et al. (2005), Geophysical evidence from the melt area for compositional controls on oceanic plates, *Nature*, *437*, 249–252, doi:10.1038/nature04014.
- Faul, U. H., and I. Jackson (2005), The seismological signature of temperature and grain size variations in the upper mantle, *Earth Planet. Sci. Lett.*, *234*, 119–134, doi:10.1016/j.epsl.2005.02.008.
- Fischer, K. M., H. A. Ford, D. L. Abt, and C. A. Rychert (2010), The lithosphere-asthenosphere boundary, *Annu. Rev. Earth Planet. Sci.*, *38*, 551–575, doi:10.1146/annurev-earth-040809-152438.
- Flanagan, M. P., and P. M. Shearer (1998), Global mapping of topography on transition zone velocity discontinuities by stacking SS precursors, *J. Geophys. Res.*, *103*, 2673–2692, doi:10.1029/97JB03212.
- Gaherty, J. B., M. Kato, and T. H. Jordan (1999), Seismological structure of the upper mantle: A regional comparison of seismic layering, *Phys. Earth Planet. Inter.*, *110*, 21–41, doi:10.1016/S0031-9201(98)00132-0.
- Gu, Y. J., and A. M. Dziewonski (2002), Global variability of transition zone thickness, *J. Geophys. Res.*, *107*(B7), 2135, doi:10.1029/2001JB000489.
- Gu, Y. J., S. C. Webb, A. Lerner-Lam, and J. B. Gaherty (2005), Upper mantle structure beneath the eastern Pacific Ocean ridges, *J. Geophys. Res.*, *110*, B06305, doi:10.1029/2004JB003381.
- Gung, Y. C., M. Panning, and B. Romanowicz (2003), Global anisotropy and the thickness of continents, *Nature*, *422*, 707–711, doi:10.1038/nature01559.
- Gutenberg, B. (1948), On the layer of relatively low wave velocity at a depth of about 80 km, *Bull. Seismol. Soc. Am.*, *38*, 121–148.
- Harmon, N., D. W. Forsyth, and D. S. Weeraratne (2009), Thickening of young Pacific lithosphere from high-resolution Rayleigh wave tomography: A test of the conductive cooling model, *Earth Planet. Sci. Lett.*, *278*, 96–106, doi:10.1016/j.epsl.2008.11.025.
- Heit, B., F. Sodoudi, X. Yuan, M. Bianchi, and R. Kind (2007), An S receiver function analysis of the lithospheric structure in South America, *Geophys. Res. Lett.*, *34*, L14307, doi:10.1029/2007GL030317.
- Heit, B., X. Yuan, M. Bianchi, R. Kind, and J. Gossler (2010), Study of the lithospheric and upper-mantle discontinuities beneath eastern Asia by SS precursors, *Geophys. J. Int.*, *183*, 252–266, doi:10.1111/j.1365-246X.2010.04714.x.
- Hirano, N., et al. (2006), Volcanism in response to plate flexure, *Science*, *313*, 1426–1428, doi:10.1126/science.1128235.
- Hirschmann, M. M. (2010), Partial melt in the oceanic low velocity zone, *Phys. Earth Planet. Inter.*, *179*, 60–71, doi:10.1016/j.pepi.2009.12.003.
- Hirth, G., and D. L. Kohlstedt (1996), Water in the oceanic upper mantle: Implications for rheology, melt extraction, and the evolution of the lithosphere, *Earth Planet. Sci. Lett.*, *144*, 93–108, doi:10.1016/0012-821X(96)00154-9.
- Holtzman, B. K., et al. (2003), Melt segregation and strain partitioning: Implications for seismic anisotropy and mantle flow, *Science*, *301*, 1227–1230, doi:10.1126/science.1087132.
- Houser, C., G. Masters, M. Flanagan, and P. Shearer (2008), Determination and analysis of long-wavelength transition zone structure using SS precursors, *Geophys. J. Int.*, *174*, 178–194, doi:10.1111/j.1365-246X.2008.03719.x.
- Jordan, T. H. (1981), Global tectonic regionalization for seismological data analysis, *Bull. Seismol. Soc. Am.*, *71*, 1131–1141.
- Karato, S. (2003), Mapping water content in the upper mantle, in *Inside the Subduction Factory*, *Geophys. Monogr. Ser.*, vol. 128, edited by J. Eiler, pp. 135–152, AGU, Washington, D. C.
- Karato, S. (2010), Rheology of the Earth's mantle: A historical review, *Gondwana Res.*, *18*, 17–45, doi:10.1016/j.gr.2010.03.004.
- Katz, R. F. (2010), Porosity-driven convection and asymmetry beneath mid-ocean ridges, *Geochem. Geophys. Geosyst.*, *11*, Q0AC07, doi:10.1029/2010GC003282.
- Kawakatsu, H., et al. (2009), Seismic evidence for sharp lithosphere-asthenosphere boundaries of oceanic plates, *Science*, *324*, 499–502.
- Kohlstedt, D. L., and B. K. Holtzman (2009), Shearing melt out of the Earth: An experimentalist's perspective on the influence of deformation on melt extraction, *Annu. Rev. Earth Planet. Sci.*, *37*, 561–593, doi:10.1146/annurev.earth.031208.100104.
- Korenaga, T., and J. Korenaga (2008), Subsidence of normal oceanic lithosphere, apparent thermal expansivity, and seafloor flattening, *Earth Planet. Sci. Lett.*, *268*, 41–51, doi:10.1016/j.epsl.2007.12.022.
- Kumar, P., and H. Kawakatsu (2011), Imaging the seismic lithosphere-asthenosphere boundary of the oceanic plate, *Geochem. Geophys. Geosyst.*, *12*, Q01006, doi:10.1029/2010GC003358.
- Kumar, P., et al. (2005), The lithosphere-asthenosphere boundary in the northwest Atlantic region, *Earth Planet. Sci. Lett.*, *236*, 249–257, doi:10.1016/j.epsl.2005.05.029.
- Kuo, B. Y., D. F. Forsyth, and E. M. Parmentier (1986), Flexure and thickening of the lithosphere at the East Pacific Rise, *Geophys. Res. Lett.*, *13*, 681–684, doi:10.1029/GL013i007p00681.
- Lawrence, J. F., and P. M. Shearer (2008), Imaging mantle transition zone thickness with SdS-SS finite-frequency sensitivity kernels, *Geophys. J. Int.*, *174*, 143–158, doi:10.1111/j.1365-1246X.2007.03673.x.
- Li, X., R. Kind, K. Priestley, S. V. Sobolev, F. Tilmann, X. Yuan, and M. Weber (2000), Mapping the Hawaiian plume conduit with converted seismic waves, *Nature*, *405*, 938–941, doi:10.1038/35016054.
- Li, X. Q., R. Kind, X. H. Yuan, I. Wolber, and W. Hanka (2004), Rejuvenation of the lithosphere by the Hawaiian plume, *Nature*, *427*, 827–829, doi:10.1038/nature02349.
- Maggi, A., E. Debayle, K. Priestley, and G. Barruol (2006), Multimode surface waveform tomography of the Pacific Ocean: A closer look at the lithospheric cooling signature, *Geophys. J. Int.*, *166*, 1384–1397, doi:10.1111/j.1365-246X.2006.03037.x.
- Mierdel, K., H. Keppler, J. R. Smyth, and F. Langenhorst (2007), Water solubility in aluminous orthopyroxene and the origin of Earth's asthenosphere, *Science*, *315*, 364–368, doi:10.1126/science.1135422.
- Müller, R. D., M. Sdrolias, C. Gai, and W. R. Roest (2008), Age, spreading rates, and spreading asymmetry of the world's ocean crust, *Geochem. Geophys. Geosyst.*, *9*, Q04006, doi:10.1029/2007GC001743.
- Nettles, M., and A. M. Dziewoński (2008), Radially anisotropic shear velocity structure of the upper mantle globally and beneath North America, *J. Geophys. Res.*, *113*, B02303, doi:10.1029/2006JB004819.
- Nishimura, C. E., and D. W. Forsyth (1989), The anisotropic structure of the upper mantle in the Pacific, *Geophys. J. Int.*, *96*, 203–229.
- Parsons, B., and J. G. Sclater (1977), Analysis of variation of ocean-floor bathymetry and heat-flow with age, *J. Geophys. Res.*, *82*, 803–827, doi:10.1029/JB082i005p00803.
- Priestley, K., and D. McKenzie (2006), The thermal structure of the lithosphere from shear wave velocities, *Earth Planet. Sci. Lett.*, *244*, 285–301, doi:10.1016/j.epsl.2006.01.008.
- Ritzwoller, M. H., N. M. Shapiro, and S. J. Zhong (2004), Cooling history of the Pacific lithosphere, *Earth Planet. Sci. Lett.*, *226*, 69–84, doi:10.1016/j.epsl.2004.07.032.
- Rychert, C. A., and P. M. Shearer (2009), A global view of the lithosphere-asthenosphere boundary, *Science*, *324*, 495–498, doi:10.1126/science.1169754.
- Rychert, C. A., and P. M. Shearer (2010), Resolving crustal thickness using SS waveform stacks, *Geophys. J. Int.*, *180*, 1128–1137, doi:10.1111/j.1365-246X.2009.04497.x.

- Rychert, C. A., K. M. Fischer, and S. Rondenay (2005), A sharp lithosphere-asthenosphere boundary imaged beneath eastern North America, *Nature*, *436*, 542–545, doi:10.1038/nature03904.
- Rychert, C. A., S. Rondenay, and K. M. Fischer (2007), P-to-S and S-to-P imaging of a sharp lithosphere-asthenosphere boundary beneath eastern North America, *J. Geophys. Res.*, *112*, B08314, doi:10.1029/2006JB004619.
- Rychert, C. A., P. M. Shearer, and K. M. Fischer (2010), Scattered wave imaging of the lithosphere-asthenosphere boundary, *Lithos*, *120*, 173–185, doi:10.1016/j.lithos.2009.12.006.
- Shearer, P. M. (1991), Constraints on upper mantle discontinuities from observations of long-period reflected and converted phases, *J. Geophys. Res.*, *96*, 18,147–18,182, doi:10.1029/91JB01592.
- Shearer, P. M. (1996), Transition zone velocity gradients and the 520 km discontinuity, *J. Geophys. Res.*, *101*, 3053–3066, doi:10.1029/95JB02812.
- Smith, W. H. F., and D. T. Sandwell (1997), Global sea floor topography from satellite altimetry and ship depth soundings, *Science*, *277*, 1956–1962, doi:10.1126/science.277.5334.1956.
- Sparks, D., and E. Parmentier (1991), Melt extraction from the mantle beneath spreading centers, *Earth Planet. Sci. Lett.*, *105*, 368–377, doi:10.1016/0012-821X(91)90178-K.
- Stein, C. A., and S. Stein (1992), A model for the global variation in oceanic depth and heat-flow with lithospheric age, *Nature*, *359*, 123–129, doi:10.1038/359123a0.
- Stixrude, L., and C. Lithgow-Bertelloni (2005), Mineralogy and elasticity of the oceanic upper mantle: Origin of the low-velocity zone, *J. Geophys. Res.*, *110*, B03204, doi:10.1029/2004JB002965.
- Takei, Y. (2002), Effect of pore geometry on V_p/V_s : From equilibrium geometry to crack, *J. Geophys. Res.*, *107*(B2), 2043, doi:10.1029/2001JB000522.
- Takei, Y., and B. K. Holtzman (2009), Viscous constitutive relations of solid-liquid composites in terms of grain boundary contiguity: 1. Grain boundary diffusion control model, *J. Geophys. Res.*, *114*, B06205, doi:10.1029/2008JB005850.
- Tan, Y., and D. V. Helmberger (2007), Trans-Pacific upper mantle shear velocity structure, *J. Geophys. Res.*, *112*, B08301, doi:10.1029/2006JB004853.
- Vinnik, L. P., G. R. Foulger, and Z. Du (2005), Seismic boundaries in the mantle beneath Iceland: A new constraint on temperature, *Geophys. J. Int.*, *160*, 533–538, doi:10.1111/j.1365-246X.2005.02529.x.
- Watts, A. (1978), Analysis of isostasy in the world's oceans: 1. Hawaiian-Emperor seamount chain, *J. Geophys. Res.*, *83*, 5989–6004, doi:10.1029/JB083iB12p05989.

C. A. Rychert, Department of Earth Science, University of Bristol, Wills Memorial Building, Queen's Road, Bristol BS8 1RJ, UK. (Kate.Rychert@bristol.ac.uk)

P. M. Shearer, Institute of Geophysics and Planetary Physics, Scripps Institution of Oceanography, University of California, San Diego, 9500 Gilman Dr., M/C 0225, La Jolla, CA 92093, USA.